



NOTICE: WARNING CONCERNING COPYRIGHT RESTRICTIONS

The copyright law of the United States (Title 17, United States Code) governs the making of photocopies or other reproductions of copyrighted material.

Under certain conditions specified in the law, libraries and archives are authorized to furnish a photocopy or other reproduction. One of these specific conditions is that the photocopy or reproduction is not to be “used for any purpose other than private study, scholarship, or research.” If a user makes a request for, or later uses, a photocopy or reproduction for purposes in excess of “fair use,” that user may be liable for copyright infringement.

This institution reserves the right to refuse to accept a copying order if, in its judgment, fulfillment of the order would involve violation of copyright law.

Ultrasmall nanoparticles induce ferroptosis in nutrient-deprived cancer cells and suppress tumour growth

Sung Eun Kim^{1,2}, Li Zhang³, Kai Ma⁴, Michelle Riegman¹, Feng Chen³, Irina Ingold⁵, Marcus Conrad⁵, Melik Ziya Turker⁴, Minghui Gao¹, Xuejun Jiang^{1,2}, Sebastien Monette⁶, Mohan Pauliah³, Mithat Gonen⁷, Pat Zanzonico⁸, Thomas Quinn⁹, Ulrich Wiesner⁴, Michelle S. Bradbury^{3,10*†} and Michael Overholtzer^{1,2*†}

The design of cancer-targeting particles with precisely tuned physicochemical properties may enhance the delivery of therapeutics and access to pharmacological targets. However, a molecular-level understanding of the interactions driving the fate of nanomedicine in biological systems remains elusive. Here, we show that ultrasmall (<10 nm in diameter) poly(ethylene glycol)-coated silica nanoparticles, functionalized with melanoma-targeting peptides, can induce a form of programmed cell death known as ferroptosis in starved cancer cells and cancer-bearing mice. Tumour xenografts in mice intravenously injected with nanoparticles using a high-dose multiple injection scheme exhibit reduced growth or regression, in a manner that is reversed by the pharmacological inhibitor of ferroptosis, lipoxstatin-1. These data demonstrate that ferroptosis can be targeted by ultrasmall silica nanoparticles and may have therapeutic potential.

Nanomaterials designed to target cancer may hold therapeutic potential by enhancing the delivery of therapeutics^{1–4}, but their interactions with cancer in animal models and their long-term effects on cells remain poorly understood^{5–9}. To examine the effects of nanoparticle ingestion on cells, we used ~6 nm surface-functionalized poly(ethylene glycol)-coated (PEGylated) near-infrared (NIR) fluorescent silica nanoparticles, referred to as Cornell dots (C dots), with diameters controllable down to the sub-10 nm range, as reported in detail elsewhere¹⁰. This FDA Investigational New Drug (IND)-approved hybrid organo-silica particle was previously shown to be a promising cancer molecular imaging agent in metastatic melanoma patients after functionalizing its surface with $\alpha_v\beta_3$ -integrin-targeting peptides and radiolabels^{2,11}. Preferential accumulation was observed within integrin-expressing primary and/or metastatic melanomatous lesions in human subjects and animal melanoma models^{11,12}, while at the same time demonstrating rapid renal clearance.

Given its potential clinical utility and its early adaptation for drug delivery applications¹³, we initially performed detailed cell biological studies using the latest generation of C dots, synthesized in water, referred to as C' dots¹⁰, surface-functionalized with a 14 mer peptide analogue, alpha-melanocyte stimulating hormone (α MSH)¹⁴, which targets a different surface receptor expressed on malignant melanoma cells (melanocortin-1 receptor, MC1-R). The resulting α MSH-PEG-C' dots (Fig. 1a) were used here to determine whether alterations in cell survival occurred in cancer cell lines

and tumour xenografts over a wide dose range relative to that seen under control conditions and whether cellular pathways were modulated by particle ingestion.

α MSH-PEG-C' dots reside in lysosomes and are well tolerated

Live imaging of MC1-R-expressing human melanoma cells (M21) treated with particles for 24 h revealed co-localization of fluorescent α MSH-PEG-C' dots with lysosomes, the latter visualized by expression of a green fluorescent protein (GFP)-tagged lysosomal-associated membrane protein 1 (LAMP1), indicating that ingested particles reside in lysosomal or late endosomal networks (Fig. 1b). M21 cells treated with increasing concentrations of α MSH-PEG-C' dots up to 15 μ M showed similar survival and proliferation rates to control cells (Fig. 2a), demonstrating that incubation at even high particle concentrations is well tolerated. We next examined if lysosomes were functioning properly within cells treated with α MSH-PEG-C' dots. To determine this, we examined the autophagy pathway, which targets intracellular substrates for lysosomal degradation. Autophagy was examined by quantifying the basal levels and turnover rates of the autophagy protein microtubule-associated protein 1 light chain 3 (LC3), which is lipidated onto autophagosomal membranes and becomes degraded following the fusion of autophagosomes with lysosomes¹⁵. The accumulation of the autophagosome-associated, lipidated form of LC3, or LC3-II, identified by its faster electrophoretic mobility in SDS-polyacrylamide gel

¹Cell Biology Program, Sloan Kettering Institute for Cancer Research, New York, New York 10065, USA. ²BCMB Allied Program, Weill Cornell Medical College, New York, New York 10065, USA. ³Department of Radiology, Sloan Kettering Institute for Cancer Research, New York, New York 10065, USA.

⁴Department of Materials Science & Engineering, Cornell University, Ithaca, New York 14853, USA. ⁵Helmholtz Zentrum München, Institute of Developmental Genetics, 85764 Neuherberg, Germany. ⁶Tri-Institutional Laboratory of Comparative Pathology, The Rockefeller University, Sloan Kettering Institute for Cancer Research, Weill Cornell Medical College, New York, New York 10065, USA. ⁷Department of Epidemiology and Biostatistics, Sloan Kettering Institute for Cancer Research, New York, New York 10065, USA. ⁸Department of Medical Physics, Sloan Kettering Institute for Cancer Research, New York, New York 10065, USA. ⁹Department of Biochemistry, University of Missouri, Columbia, Missouri 65211, USA. ¹⁰Molecular Pharmacology Program, Sloan Kettering Institute for Cancer Research, New York, New York 10065, USA. [†]These authors contributed equally to this work.

*e-mail: overhom1@mskcc.org; bradburm@mskcc.org

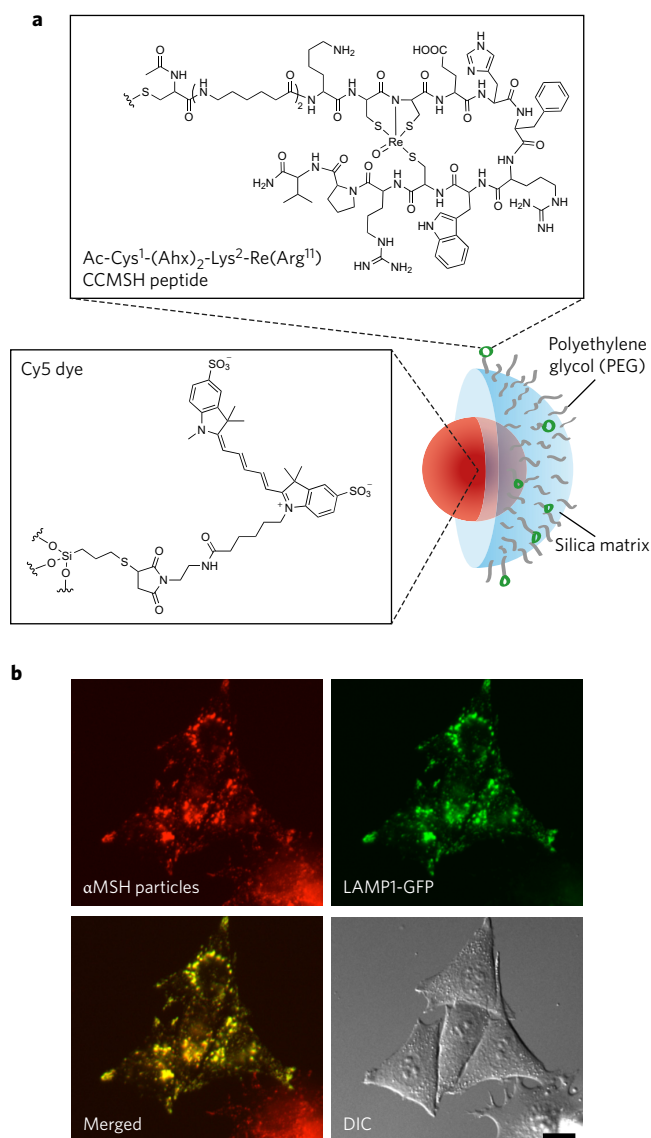


Figure 1 | αMSH-PEG-C' dot particles and their localization to lysosomal networks. **a**, Silica-based and ultrasmall αMSH-PEG-C' dots of 6-nm-diameter silica-based particles with a fluorescent (Cy5 encapsulated) core and polyethylene glycol (PEG) coating and alpha melanocyte-stimulating hormone (αMSH)-modified exterior. **b**, αMSH-PEG-C' dots localize to lysosomal networks in cells. M21 melanoma cells expressing LAMP1-GFP (green) were treated with αMSH-PEG-C' dots (15 μM) for 24 h. Note co-localization between nanoparticles (Cy5 fluorescence, pseudo-coloured red) and LAMP1-GFP in the merged image. Scale bar, 10 μm.

electrophoresis (PAGE) relative to the non-lipidated form, LC3-I, can be quantified as a measure of autophagy induction or flux through lysosomes¹⁵. Cells treated with increasing concentrations of αMSH-PEG-C' dots for 24 h, from 0.15 to 15 μM, had similar relative LC3-II levels as control cells, suggesting that autophagy is not induced or perturbed by nanoparticle treatment (Fig. 2b). Importantly, the treatment of cells with a lysosomal inhibitor, concanamycin A (ConA), which inhibits lysosome function by raising pH, and blocks autophagosome degradation, resulted in a similar accumulation of LC3-II in particle-treated cells as compared to controls, demonstrating that lysosomes are functioning properly even when cells are loaded with high concentrations of αMSH-PEG-C' dots (Fig. 2b).

αMSH-PEG-C' dots induce death of starved cells

Although αMSH-PEG-C' dots were well tolerated by cells cultured under nutrient-replete conditions and the autophagy pathway and lysosome function appeared to be unperturbed, we further examined if particle treatment might affect cells cultured under nutrient-deprived conditions where autophagy is induced. Cells cultured in amino-acid-free media were treated with αMSH-PEG-C' dots and examined by time-lapse imaging. Although amino-acid deprivation was well tolerated by M21 cells in the absence of particles, the treatment of amino-acid-deprived cells with 15 μM αMSH-PEG-C' dots, which had no effect on cells in nutrient-replete media, surprisingly led to cell death at high rates, detected by the uptake of Sytox Green, a membrane-impermeable nucleic acid dye that labels cells with ruptured plasma membranes (Fig. 2c). This demonstrates that while αMSH-PEG-C' dots are generally well tolerated, nutrient-deprived cancer cells are sensitive to treatment. To determine whether this finding could have consequences for tumour growth *in vivo*, we incubated M21 cells with αMSH-PEG-C' dots in culture under nutrient-replete conditions, which had no effect on cell viability (Fig. 2a and Supplementary Fig. 1a), and then injected particle-exposed cells, as well as particle-unexposed cells, into mice as flank tumour xenografts, to promote a nutrient-deprived state that is known to result from a lack of vascularization in early xenograft tumours¹⁶. M21 cells loaded with αMSH-PEG-C' dots demonstrated statistically significant growth inhibition ($P < 0.001$) relative to non-particle-exposed cells (Fig. 2d). In fact, no measurable tumour growth occurred from particle-exposed cells up to 10 days following cell injection. These findings suggested that treatment with αMSH-PEG-C' dots at high concentrations may induce cell death under conditions of nutrient deprivation in culture and *in vivo*.

αMSH-PEG-C' dot-induced death occurs by ferroptosis

We sought to identify the mechanism of how cells treated with αMSH-PEG-C' dots undergo cell death under nutrient-deprived conditions. Careful inspection of the morphology of dying cells suggested a form of necrosis, involving cell swelling and plasma membrane rupture, in the absence of cell blebbing and fragmentation that is typically observed during apoptosis (Fig. 3a and Supplementary Fig. 1b). To more definitively identify the mechanism of cell death, we used two non-tumour cell lines, MCF10A human mammary epithelial cells and mouse embryo fibroblasts (MEF), which were also observed to die at high rates when cultured in amino-acid-free media in the presence of αMSH-PEG-C' dots (Fig. 3b). Cells rendered resistant to apoptosis, by overexpression of the anti-apoptotic protein Bcl-2 (MCF10A-Bcl2) (Supplementary Fig. 1c) or by genetic deletion of *Bax* and *Bak* (*Bax/Bak*^{-/-} MEFs)^{17,18}, underwent cell death at rates similar to control cells, suggesting that αMSH-PEG-C' dot-induced cell death does not occur by apoptosis (Fig. 3c,d). Next, we examined whether cell death was occurring by necroptosis, a programmed form of necrosis that requires the RIPK3 kinase¹⁹. *Ripk3*^{-/-} knockout MEFs, which are resistant to necroptosis (Supplementary Fig. 1d), also underwent cell death at rates similar to controls, suggesting that nanoparticle treatment does not induce necroptosis (Fig. 3e). We then determined whether a recently described form of cell death involving the autophagy pathway, autosis²⁰, could be involved, by treating autophagy-related gene 5 knockout MEFs (*Atg5*^{-/-} MEFs), completely deficient for autophagy, with αMSH-PEG-C' dots in the absence of amino acids. *Atg5*^{-/-} MEFs underwent cell death at rates similar to those of controls, demonstrating that αMSH-PEG-C' dot-induced cell death does not involve autophagy and is not autosis (Fig. 3e). Collectively, the foregoing data demonstrate that cell death, induced by a combination of particle treatment and amino-acid deprivation, occurs independently of apoptosis, necroptosis and autosis.

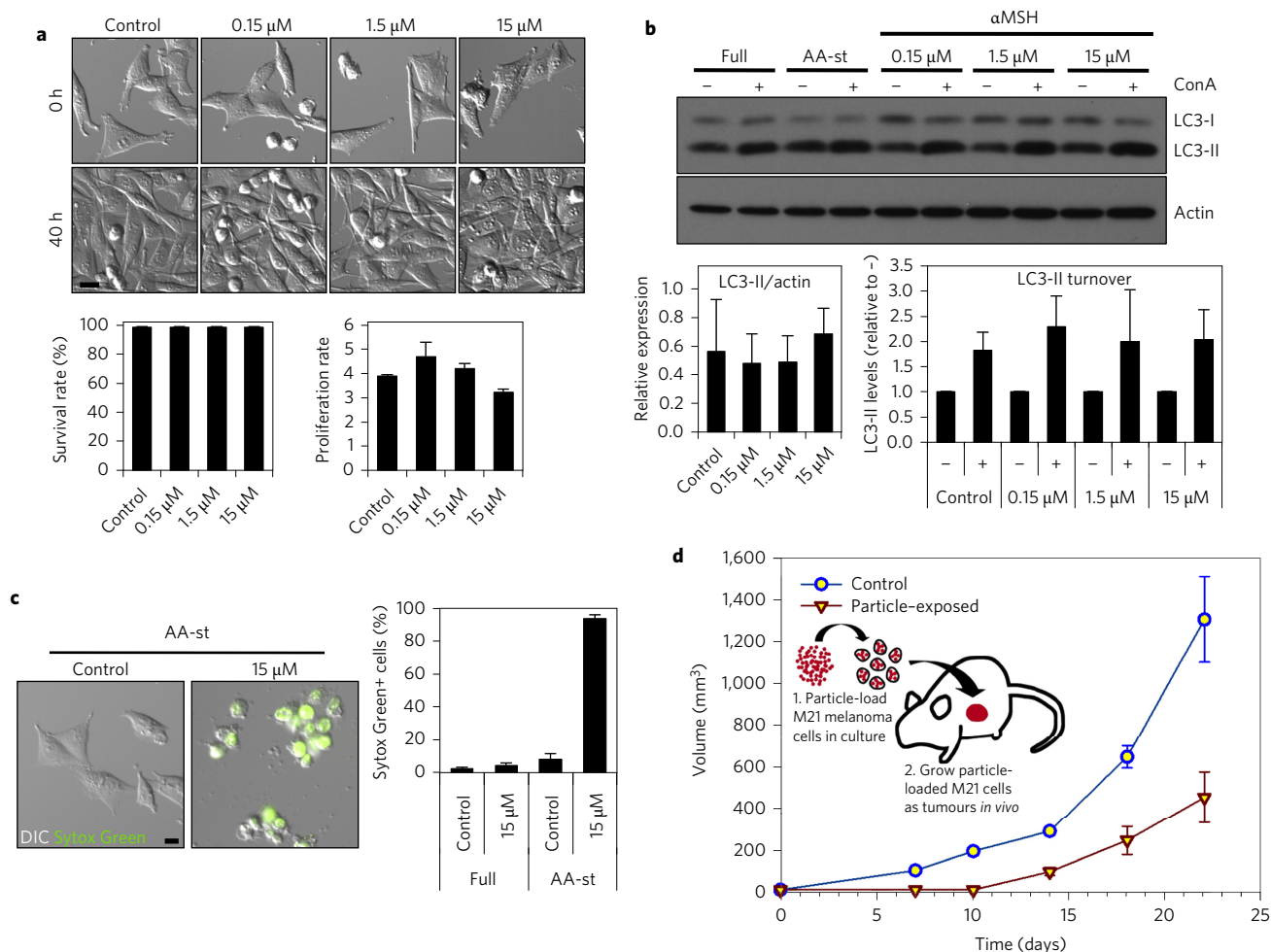


Figure 2 | α MSH-PEG-C' dot particles induce cell death in amino-acid-deprived conditions. **a**, Nanoparticles are well tolerated in nutrient-replete media. Images show M21 cells treated with the indicated α MSH-PEG-C' dot concentrations and cultured for 40 h. Nanoparticles had no significant effect on cell survival (left graph) or cell proliferation (right graph), as quantified by time-lapse microscopy-based tracking of individual cell fates. Error bars indicate mean \pm standard error of the mean. $n = 3$ biological experiments, with five independent fields of view for each. Supplementary Fig. 6a,b shows individual experimental values. Scale bar, 10 μ m. **b**, Autophagy and lysosome function in nanoparticle-treated cells are unperturbed. Western blot shows LC3-I and -II in cells treated with increasing doses of α MSH-PEG-C' dots for 24 h compared to untreated (Full media) and amino-acid-starved (AA-st) cells, in the presence (+) and absence (-) of the lysosome inhibitor concanamycin A (ConA, 1 h at 100 nM). Levels of LC3-II (left graph) are unaltered by nanoparticle treatment, and ConA-inducible LC3-II accumulation (right graph), a measure of autophagy flux, is similar in treated and untreated cells. Error bars indicate mean \pm standard error of the mean. $n = 3$ biological replicates for each group. Supplementary Fig. 6c,d shows individual experimental values. **c**, Nanoparticle treatment induces cell death of M21 cells cultured in amino-acid-free media. Images show live control cells and dead (Sytox Green+) nanoparticle-treated cells in AA-st conditions. Scale bar, 10 μ m. Graph shows percent Sytox Green+ cells in full media (Full) or AA-st conditions after 50 h, as determined by time-lapse microscopy. Error bars indicate mean \pm standard deviation. $n = 4$ for each group. Each replicate is from one biological experiment, quantified with five independent fields of view. **d**, M21 cells treated with 15 μ M α MSH-PEG-C' dots in full media for 72 h before creating xenografts in immunodeficient (SCID/Beige) mice demonstrate growth inhibition (inverted triangles) relative to untreated control cells (circles). Schematic shows workflow, consisting of (1) particle-loading M21 melanoma cells, by treatment at 15 μ M for 48 h in culture under full media conditions, and (2) injecting 5×10^6 particle-loaded M21 cells into mice to assay xenograft tumour growth versus control untreated cells. Data show mean tumour volume over 22 days of growth from three tumours per group. Error bars indicate mean \pm standard error of the mean. Particle-treated M21 cells showed statistically significant ($P < 0.001$) growth inhibition compared with untreated control cells over the study interval. P value is from a Wald test in a regression model estimated by generalized estimating equations to take into account the longitudinal nature of the data.

We next examined whether ferroptosis, a recently described cell death mechanism that occurs via an iron and lipid reactive oxygen species (ROS)-dependent process and is induced by glutathione depletion²¹, could be involved in α MSH-PEG-C'-dot-induced cell death. We first tested whether ferrostatin-1 and liproxstatin-1, pharmacological inhibitors of ferroptosis that are scavengers of lipid ROS, could block cell death in this context. Treatment with either inhibitor rescued cell viability, reducing cell death to levels occurring under amino-acid-deprived conditions in the absence of nanoparticles (Fig. 4a and Supplementary Fig. 1e). Nanoparticle-induced

cell death was also inhibited by treatment with other antioxidants, including butylated hydroxyanisole (BHA), ascorbic acid (Asc Acid) and trolox, or, alternatively, by glutathione repletion through the addition of glutathione or *N*-acetylcysteine (NAC), a precursor of glutathione (Fig. 4b). To examine whether lipid ROS accumulate during nanoparticle-induced cell death, we imaged particle-exposed cells in the presence of the lipid oxidation indicator C11-BODIPY. Increased fluorescence before cell death was seen to occur in response to treatment with the known ferroptosis-inducing agent erastin, in a liproxstatin-1-inhibitable manner (Fig. 4c and

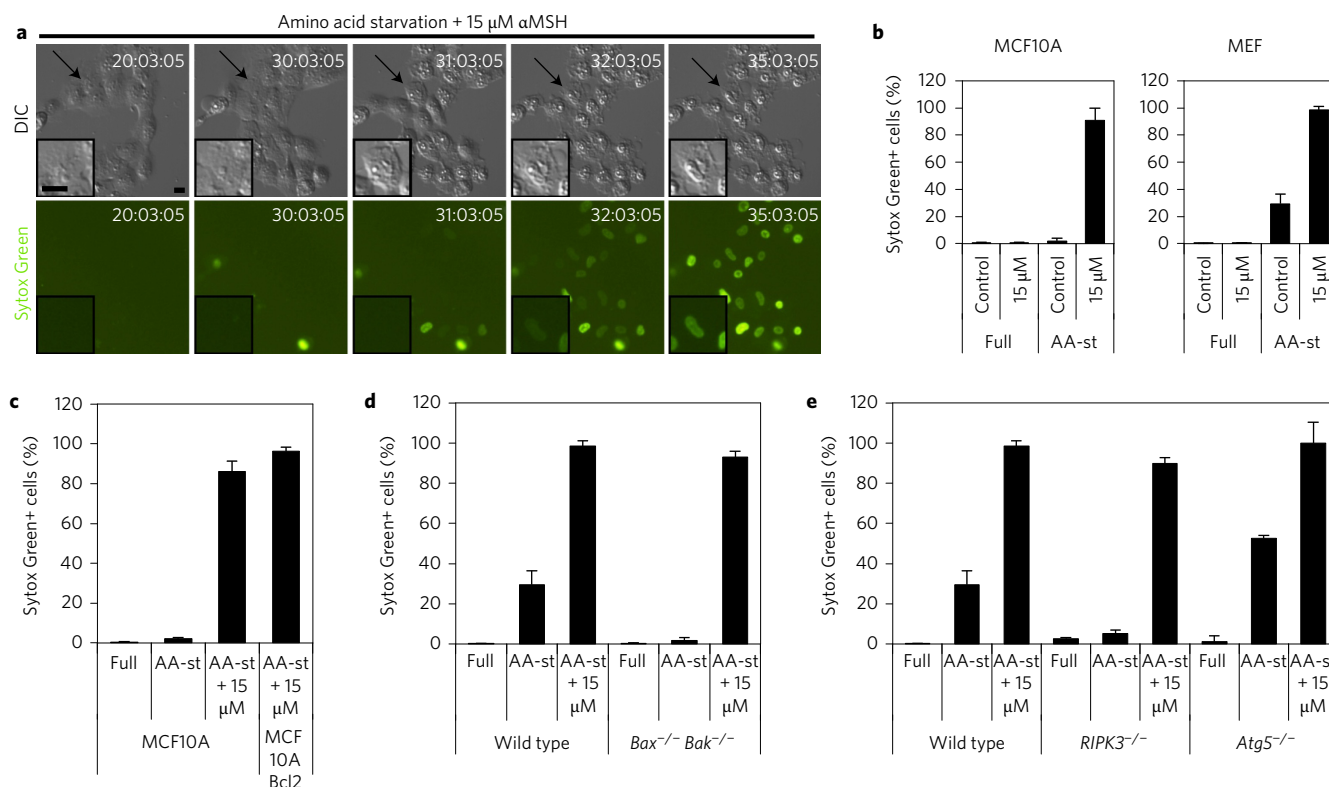


Figure 3 | $\alpha\text{MSH-PEG-C}'$ dot particle-induced cell death is not apoptosis, necroptosis or autosis. **a**, MCF10A human mammary epithelial cells cultured in the absence of amino acids with 15 μM $\alpha\text{MSH-PEG-C}'$ dots undergo cell death after 30 h with necrotic features. Insets: a dying cell, indicated by an arrow. Fluorescence images show Sytox Green-labelling of dead cell nuclei. Scale bar, 10 μm . **b**, Quantification of cell death (Sytox Green+) in MCF10A and mouse embryo fibroblast (MEF) cultures in full media or amino-acid-starved (AA-st) conditions in the presence or absence of 15 μM $\alpha\text{MSH-PEG-C}'$ dots and after 40 h (MCF10A) or 45 h (MEF), as determined by time-lapse microscopy. Error bars indicate mean \pm standard deviation. $n = 5$ per group. Each replicate is from one biological experiment, quantified with five independent fields of view. Supplementary Fig. 6f,g shows individual experimental values. **c–e**, Cell death assays, as in **b**, indicate that inhibition of apoptosis by Bcl2 overexpression in MCF10A (**c**), quantified after a 38 h time-lapse experiment, or deletion of Bax and Bak in MEF (**d**), quantified after 45 h, or inhibition of necroptosis by deletion of *ripk3* in MEF (**e**), quantified after 45 h, or inhibition of autophagy by knockout of *Atg5* in MEF after 45 h (**e**) does not inhibit cell death induced by amino-acid starvation and treatment with 15 μM $\alpha\text{MSH-PEG-C}'$ dots. Error bars indicate mean \pm standard deviation. $n = 5$ per group. Each replicate is from one biological experiment, quantified with five independent fields of view. Supplementary Fig. 6h–j shows individual experimental values.

Supplementary Fig. 1f). Like cell death induced by erastin treatment, lipid ROS detected by C11-BODIPY fluorescence accumulated several hours before the induction of cell death by nanoparticle treatment under amino-acid-free conditions (Fig. 4c). To further examine if nanoparticle-induced death is dependent on iron, a known requirement for ferroptosis, we found that cells treated with deferoxamine (DFO), an iron chelator used for treating iron overload and an agent reported to block ferroptosis²¹, almost completely inhibited cell death (Fig. 4d). Together, these data demonstrate that treatment of amino-acid-starved cells with high $\alpha\text{MSH-PEG-C}'$ dot concentrations induces ferroptosis. Interestingly, ferroptosis in this context was also observed to propagate from cell to cell in a wave-like manner (Fig. 4e and Supplementary Movie 1), unlike that found for cells undergoing other types of death, such as apoptosis (Supplementary Fig. 1g and Supplementary Movie 2). These findings suggested cell–cell communication of a death-inducing signal, similar to a recent report of ferroptosis occurring in renal tubules in response to treatment with erastin²².

$\alpha\text{MSH-PEG-C}'$ dots inhibit tumour growth

We next examined whether ferroptosis could be induced by nanoparticle treatment in a wider panel of cancer cells. Like M21 cells, BxPC3 pancreatic carcinoma cells, H1650 lung carcinoma cells, HT-1080 fibrosarcoma cells and 786-O renal carcinoma cells underwent high rates of necrosis when treated under amino-acid-free

conditions with $\alpha\text{MSH-PEG-C}'$ dots, indicating that cell death can be induced by a combination of particle treatment and nutrient deprivation in a variety of different cancer cell types (Fig. 5a–c and Supplementary Fig. 2a). Interestingly, HT-1080 cells underwent necrosis in response to nanoparticle treatment, even when cultured in full media (Fig. 5c), as well as in starvation media at tenfold lower particle concentrations (Supplementary Fig. 2b), suggesting that these cells are particularly sensitive to particle-induced ferroptosis. We further investigated whether particle-induced treatment responses could be generated in 786-O renal carcinoma and HT-1080 fibrosarcoma xenograft models. Using a multidosing delivery scheme, tumour growth was assessed over a 10-day period after three high-dose intravenous (i.v.) treatments of either targeted particle probe ($n = 5$) or 0.9% saline solution ($n = 3$) in immunosuppressed mice bearing flank 786-O or HT-1080 tumours. Relative to the rapidly increasing tumour volumes measured after injection with saline vehicle, statistically significant inhibition of tumour growth was observed with multiple-dose particle treatments for both tumour types (Fig. 6a,b), and greater for HT-1080 xenografts. Surprisingly, this was accompanied by partial tumour regression exceeding 50% for all particle-treated HT-1080 tumours (range, 57–78%; mean, 64%) within a 4–5 day interval after initial injection (Fig. 6c). At study termination, statistically significant reductions in treated tumour volumes (HT-1080: mean \sim 85%, $P < 0.001$; 786-O: mean \sim 73%, $P < 0.01$) were found

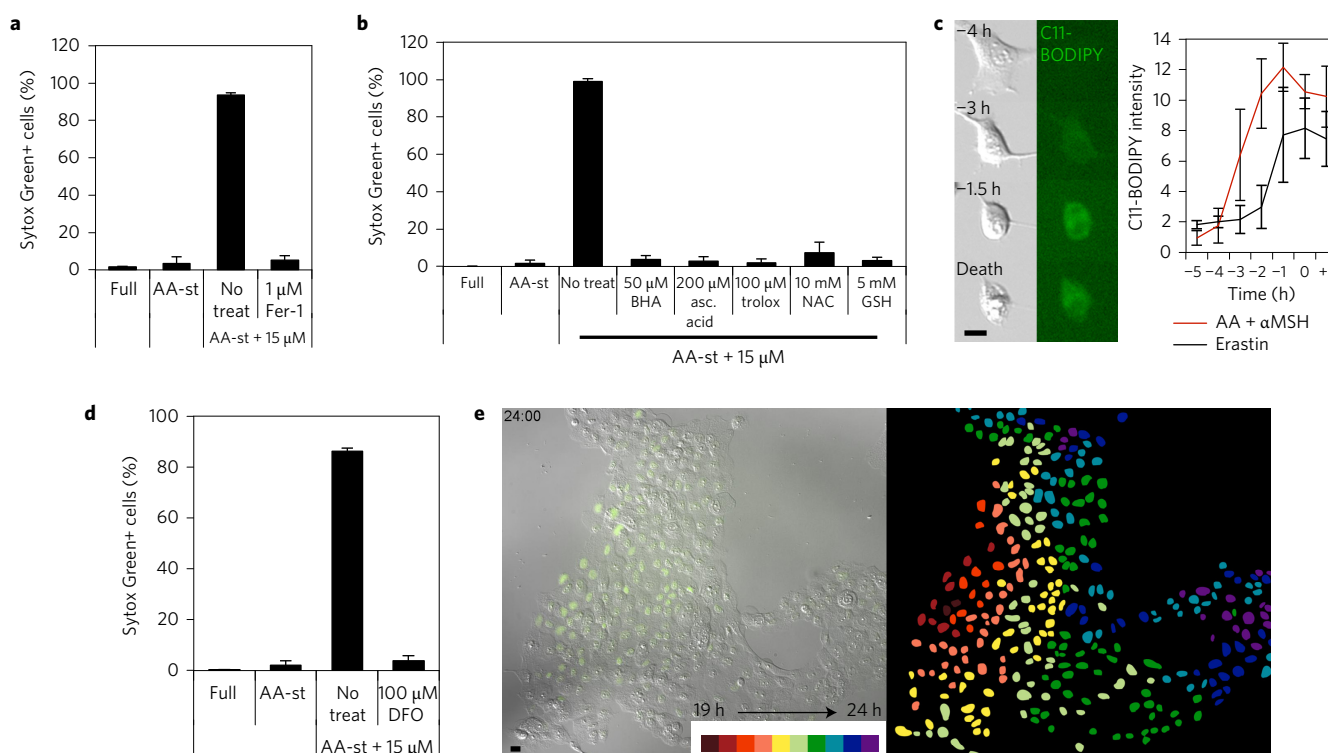


Figure 4 | Ferroptosis is the underlying mechanism of α MSH particle-induced cell death. **a**, Quantification of cell death (Sytox Green+) in MCF10A cells cultured in full media (Full) or amino-acid-starved (AA-st) conditions in the presence or absence of 15 μ M α MSH-PEG-C' dots and 1 μ M ferrostatin-1 (Fer-1) after 40 h. Error bars indicate mean \pm standard deviation. $n = 3$ per group. Each replicate is from one biological experiment, quantified with five independent fields of view. Supplementary Fig. 7a shows individual experimental values. **b**, Quantification of cell death (Sytox Green+) in MCF10A cells cultured in full media (Full) or amino-acid-starved (AA-st) conditions in the presence or absence of 15 μ M α MSH-PEG-C' dots and 50 μ M butylated hydroxyanisole (BHA), 200 μ M ascorbic acid (asc. acid), 100 μ M trolox, 10 mM *N*-acetylcysteine (NAC) or 5 mM glutathione (GSH) after 40 h. Error bars indicate mean \pm standard deviation. $n = 5$ per group. Each replicate is from one biological experiment, quantified with five independent fields of view. Supplementary Fig. 7b shows individual experimental values. **c**, Lipid ROS accumulate before death in cells treated with 15 μ M α MSH-PEG-C' dots and amino-acid withdrawal. Images show treated cells cultured in the presence of C11-BODIPY that detects lipid ROS. Note that the fluorescence intensity of C11-BODIPY increases several hours before cell death (times indicated on each image before cell death in bottom image). Scale bar, 10 μ m. Graph: quantification of C11-BODIPY fluorescence in particle-treated and amino-acid-starved cells (red line), or erastin-treated cells (black line). Mean intensities from five cells \pm standard deviation are shown for one biological experiment. Time zero indicates the time of cell death determined by DIC microscopy. Note that C11-BODIPY staining increases in intensity between 3 and 4 h before cell death. **d**, Quantification of cell death (Sytox Green+) in MCF10A cells cultured in full media (Full) or amino-acid-starved (AA-st) conditions in the presence or absence of 15 μ M α MSH-PEG-C' dots and 100 μ M deferoxamine (DFO). Error bars indicate mean \pm standard deviation. $n = 3$ per group. Each replicate is from one biological experiment, quantified with five independent fields of view. Supplementary Fig. 7c shows individual experimental values. **e**, Images from time-lapse analysis of MCF10A undergoing ferroptosis in amino-acid-starved conditions with 15 μ M α MSH-PEG-C' dots. Note that death (Sytox Green positivity) spreads cell-to-cell from the left side of the image to the right. Right image: position of each dead cell nucleus pseudocoloured to represent the relative timing of cell death. Scale bar, 10 μ m.

relative to control volumes (Fig. 6a,b). An intense fluorescence signal overlying the xenograft, obtained by whole-body optical imaging (Fig. 6d), suggested particle localization. Immunohistochemical staining for the macrophage marker Mac-2 revealed large numbers of recruited macrophages surrounding treated tumours relative to that seen around control tumours, both at low and high magnification (Fig. 6e–h).

To further examine if the inhibition of tumour growth resulting from nanoparticle treatment could be related to ferroptosis, we treated tumour-bearing mice with daily intraperitoneal (i.p.) doses of liproxstatin-1 for 10 days to determine the effects on particle-induced tumour shrinkage. Notably, in HT-1080 xenografted mice ($n = 3$) subsequently administered three high-dose particle treatments, liproxstatin-1 administration significantly reduced growth inhibition to levels nearly equivalent to those seen in non-particle-exposed tumours (Fig. 6i). Using a generalized estimating equations (GEE) model with a logit link, average daily growth in particle-exposed tumours treated with liproxstatin-1 was 14.6 mm^3 (95% confidence interval (CI): 10.1–18.9), as compared with -0.87 mm^3

(95% CI: -1.06 to -0.69) for particle treatment alone, a difference of 15.3 mm^3 (CI: 13.1–17.6; $P < 0.001$, Wald test from GEE). Corresponding particle-exposed tumour specimens were significantly smaller on average than particle-treated tumours receiving daily liproxstatin-1 (Fig. 6i, inset).

Conclusions

Here, we have demonstrated that the combined treatment of cells with α MSH-PEG-C' dots and amino-acid starvation can synergize to induce the cell death programme ferroptosis, and that high-dose particle delivery can inhibit tumour growth and cause tumour regression. These effects are reversible with liproxstatin-1. Although their role in wound repair and engulfment of cellular debris is well established, the significance of increased numbers of macrophages around particle-treated, as opposed to control tumours, remains unclear²³. It is known that a high degree of macrophage plasticity can occur in response to local cues from the tumour microenvironment²⁴ and that, upon activation, macrophages can assume a spectrum of roles needed to maintain

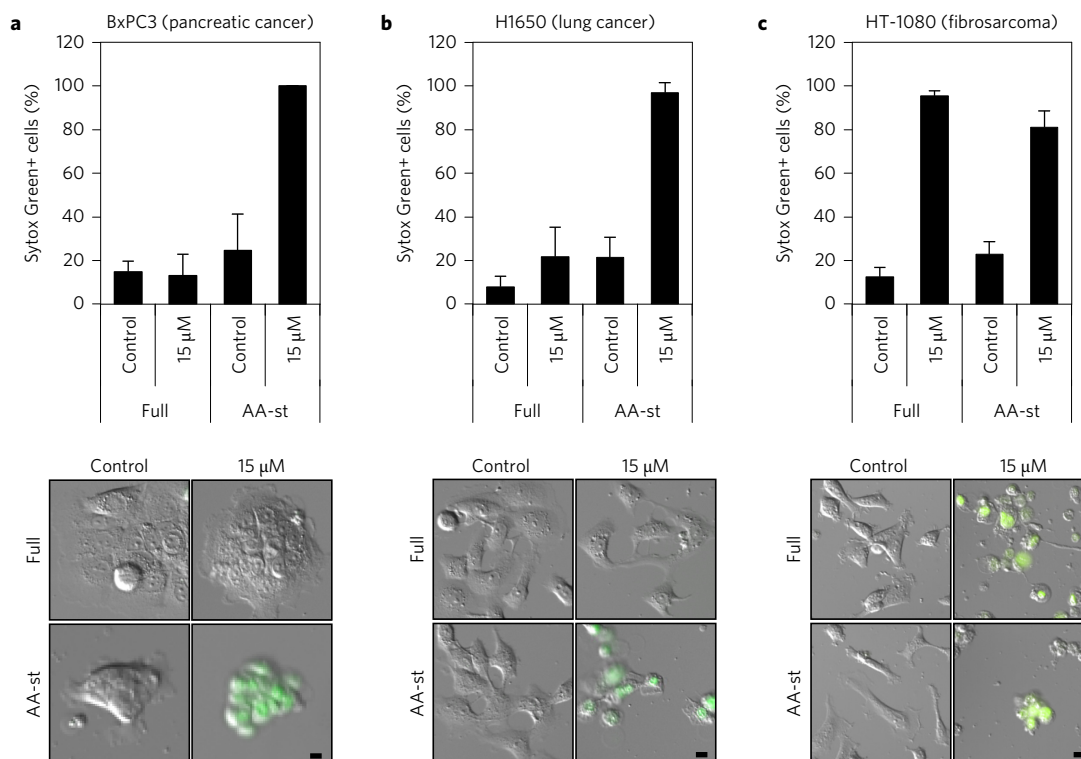


Figure 5 | α MSH-PEG-C' dots induce cell death in different types of cancer cells. **a–c**, Quantification of cell death (Sytox Green+) in BxPC3 pancreatic carcinoma cells after 40 h (**a**), H1650 lung carcinoma cells after 45 h (**b**) and HT-1080 fibrosarcoma cells after 65 h (**c**), in full media (Full) or amino-acid-free media (AA-st), in the presence or absence of 15 μ M α MSH-PEG-C' dots. Error bars indicate mean \pm standard deviation. For **a** and **b**, $n = 5$ per group. For **c**, $n = 3$ per group. Each replicate is from one biological experiment, quantified with five independent fields of view. Scale bars, 10 μ m. Supplementary Fig. 7d–f shows individual experimental values.

tissue homeostasis²⁵, including shifts in function associated with tumour shrinkage²⁴.

These data thus define a potential therapeutic application for molecularly targeted C' dots, already in clinical trials for cancer imaging and detection², but without the need for surface-attached cytotoxic agents. An important question raised by these findings is how these particles induce ferroptosis. Surface-modification of particles with α MSH peptides for targeting cancers enhances cellular internalization (data not shown). Interestingly, particle surface modification with α MSH is not required for ferroptosis in the cell lines tested. We have observed its induction, albeit more slowly, with unmodified PEGylated C' dots. The slower rate of ferroptosis induction may reflect a slower rate of internalization of unmodified particles relative to α MSH-modified platforms (Supplementary Fig. 3a).

We therefore considered that the native silica particle itself has ferroptosis-inducing activity, as deprotonated surface silanol groups and/or fractal internal structure may lead to iron adsorption and/or incorporation (that is, loading) within its structure. We indeed found iron loading of α MSH-PEG-C' dots incubated with culture media, as compared with doubly deionized water preparations (Supplementary Fig. 3b and Supplementary Table 1). Increasing amounts of iron were loaded into particles in a concentration-dependent manner following exposure to ferric oxide solutions. These findings were accompanied by a decrease in iron-loading capacity as they became saturated at high iron concentrations (Supplementary Table 1). Furthermore, increased intracellular iron levels were found for α MSH-PEG-C'-dot nanoparticle-treated cells compared to non-treated cells (Supplementary Fig. 3b and Supplementary Table 1). Consistent with a model in which particles deliver iron into cells, particle-treated cells upregulated expression of the heavy chain of ferritin (FTH1) that binds cytosolic

iron (Supplementary Fig. 3c). We further found that iron loading into cells by treatment with ferric ammonium citrate (FAC) is sufficient to mimic particle treatment and induce ferroptosis in amino-acid-starved cells (Supplementary Fig. 3d), suggesting that nanoparticles may engage ferroptosis by loading iron into cells.

Increased iron uptake could lead to the depletion of glutathione, conceivably due to increased ROS generation. We do find suppression of glutathione levels in particle-treated cells (Supplementary Fig. 3e). Pretreatment with erastin, which inhibits glutathione production by blocking cystine uptake, sensitizes cells to particle-induced ferroptosis, suggesting that glutathione depletion is rate-limiting for particle-induced death (Supplementary Fig. 3f). Taken together, our data support a model whereby particle-induced ferroptosis is executed following iron uptake into cells, suppression of glutathione, and accumulation of lipid ROS (Supplementary Fig. 4). Lipid ROS may accumulate in glutathione-suppressed cells due to lowered activity of the glutathione peroxidase 4 (GPX4) enzyme that protects cells from lipid peroxidation and inhibits ferroptosis^{26,27}. We have not found that particle treatment inhibits GPX4 activity in an enzymatic assay from treated cell lysates (Supplementary Fig. 3g), consistent with the model that particle treatment does not lead to lipid peroxidation by direct inhibition of GPX4. We additionally note that particle-induced ferroptosis does not require the presence of glutamine, unlike ferroptosis occurring in starved cells²⁸, as our studies also use amino-acid-free conditions in which enhanced iron uptake may bypass the requirement for glutamine.

The concentration of nanoparticles used here to either induce *in vitro* cell death or inhibit *in vivo* tumour growth is at least four orders of magnitude higher than what is used currently in human subjects for single-dose imaging-based studies², but local concentrations could be driven to much higher levels at tumour sites as part of a

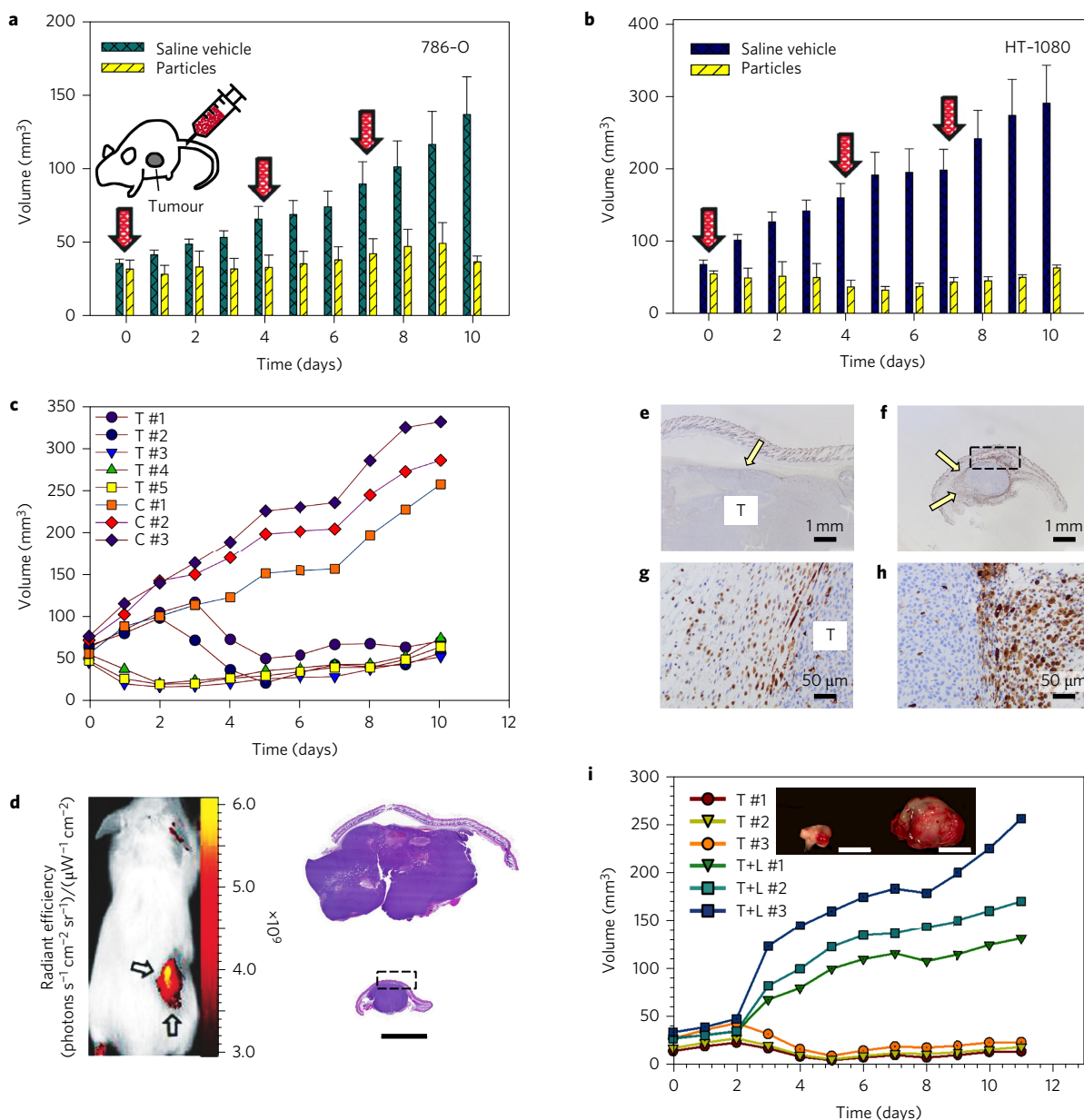


Figure 6 | α MSH-PEG-C' dots inhibit tumour growth in 786-O and HT-1080 xenograft models. **a,b**, Graphical summary of 786-O (**a**) and HT-1080 (**b**) average tumour volume measurements in α MSH-PEG-C'-dot-treated ('Particles'; $n = 5$) and control ('Saline vehicle'; $n = 3$) mice; error bars indicate standard deviation. Three high-dose (12 nmol per dose) α MSH-PEG-C' dot or saline vehicle control treatments (30 μ mol per dose) were i.v. injected (arrows) over a 10 day period, with particle-treated tumours, on average, demonstrating growth inhibition, greater for HT-1080, relative to saline-treated controls. **c**, Individual HT-1080 tumour volume measurements from **b**, shown for particle-treated ('T') and saline-treated ('C') mice. Relative to control tumour volumes, data show marked inhibition of tumour growth and partial tumour regression after particle treatments (HT-1080: $P < 0.001$; 786-OL: $P < 0.01$). P values are from a Wald test in a regression model estimated by GEEs to take into account the longitudinal nature of the data. **d**, Left: whole-body Cy5 fluorescent imaging of a representative HT-1080 tumour xenograft (arrows). Right: low-power view of H&E-stained tissue sections from representative control (top) and treated (bottom) tumours, revealing a densely cellular and invasive neoplasm exhibiting multifocal necrosis. Control specimens are noted to be disproportionately larger in size than the corresponding treated ones, without evident morphological differences. **e-h**, Immunohistochemical staining of tumour sections with macrophage marker Mac-2 shows scattered macrophages (arrow) surrounding control tumour sections (T) on low (**e**) and high (**g**) power views, while corresponding low (**f**) and high (**h**) power views of Mac-2-stained treated sections show large numbers of Mac-2-positive cells circumscribing the tumour at similar locations (boxes and arrows: **d,f**). Small numbers of intratumoural Mac-2-positive cells are also noted. **i**, Graphical summary of individual HT-1080 tumour volume measurements in mice undergoing combined inhibitor (liproxstatin-1) and particle treatment (T + L; $n = 3$) versus particle treatment alone (T; $n = 3$). Three high-dose (12 nmol per dose) α MSH-PEG-C' dot treatments (with and without i.p.-injected liproxstatin-1) were given over a 10 day period. Relative to particle treatment alone, marked progression of tumour growth is seen following combined inhibitor and particle treatment ($P < 0.001$). Image: representative particle-exposed tumours reveal specimens to be disproportionately larger in size when additionally treated with liproxstatin-1 (right tumour). Scale bars, 1 mm (**d-f**), 50 μ m (**g,h**), 1 cm (**i**).

multidosing strategy, combinatorial treatment regimen and/or by direct catheter infusion at the target site. Such a dosing schedule would be designed to yield maximum tumour-to-background ratios

while reducing off-target toxicities and promoting efficient renal clearance. It is notable that the leakiness of tumour vasculature is thought to allow the accumulation of systemically injected nanoparticles in

tumour tissues²⁹, while contributing to nutrient deprivation within tumours, suggesting that the synergism between nanoparticles and nutrient deprivation may be restricted to tumour sites *in vivo*. Some cancers may also be particularly sensitive to this mechanism of cell death, which could lower the threshold of particle concentration needed to achieve an antitumour effect. Indeed, we have found that HT-1080 cancer cells undergo α MSH-PEG-C'-dot-induced ferroptosis, even under nutrient-replete conditions (Fig. 5c), and these cells are also killed in amino-acid-deprived conditions with tenfold lower nanoparticle concentration (Supplementary Fig. 2b). It is notable that HT-1080 tumours are well vascularized (Supplementary Fig. 5a), suggesting that the sensitivity of these cancer cells to particle-induced death, even under nutrient-replete conditions (Fig. 5c), may contribute to the strong antitumour effect that is observed following intravenous particle delivery.

Although, conceivably, the sensitivity of some cancers could lower the particle concentrations needed to exert an antitumour effect, we have also found that multiple high-dose α MSH-PEG-C'-dot treatments are well tolerated. Evaluation of tumour, hepatic, renal and haematological specimens from particle- and vehicle-treated HT-1080- and 786-O-bearing mice, performed at the termination of the study, showed no significant group differences in complete blood counts, serum chemistries and hepatic and renal histopathology, with the exception of indirect and total bilirubin serum concentrations, which were moderately elevated in particle-treated mice compared with controls (Supplementary Tables 2 and 3). However, no mechanism could be ascribed to this finding given the lack of haemolysis on complete blood counts and absence of liver injury on histopathology and serum chemistries. The extent of macrophage staining among particle-treated and vehicle-treated tumour specimens is summarized in Supplementary Table 4.

The discovery of nanoparticle-induced ferroptosis as a redox modulator of cell fate, as well as a mediator of tumour regression and growth inhibition, suggests that it may be possible to exploit this process therapeutically to synchronously and selectively kill those cancers most susceptible to this mechanism. Elucidating the basis for such differential tumour sensitivity is essential. It will be important, for instance, to assess the extent of tumour vascularity, as this parameter will critically influence particle delivery, nutrient and oxygenation status and treatment response. As such, its assessment across a variety of pre-clinical tumour types may enable better screening of models suitable for the induction of cell death by this mechanism, as well as for stratifying patients in the future to appropriate combinatorial treatment paradigms.

It will also be critical to determine whether controlled variations in C'-dot properties—structure, composition or surface chemistry—enhance, or even abrogate, the induction of ferroptosis. We found, for instance, that C' dot size plays a critical role in the magnitude of the effect observed under amino-acid-deprived conditions (Supplementary Fig. 5b). Smaller-diameter (~6 nm) PEGylated C' dots led to significantly higher percentages of Sytox Green-labelled HT-1080 cells (that is, 80%) than found for larger-diameter (~10 nm) C' dots (~25%).

Finally, we note that although the response to liproxstatin-1 provides evidence for ferroptosis as an antitumour mechanism *in vivo*, other mechanisms may be contributory, including modulation of the tumour microenvironment, given the marked macrophage recruitment to particle-treated tumours (Fig. 6g,h, HT-1080; Supplementary Fig. 5c, 786-O)²⁴, an area under active investigation. Together, our findings lay the groundwork for exploiting these ultrasmall silica nanoparticles as effective ferroptosis-inducing agents in sensitive tumours.

Methods

Methods and any associated references are available in the [online version of the paper](#).

Received 7 June 2015; accepted 5 August 2016;
published online 26 September 2016

References

- Davis, M. E., Chen, Z. G. & Shin, D. M. Nanoparticle therapeutics: an emerging treatment modality for cancer. *Nat. Rev. Drug Discov.* **7**, 771–782 (2008).
- Phillips, E. *et al.* Clinical translation of an ultrasmall inorganic optical-PET imaging nanoparticle probe. *Sci. Transl. Med.* **6**, 260ra149 (2014).
- Duncan, R. & Richardson, S. C. Endocytosis and intracellular trafficking as gateways for nanomedicine delivery: opportunities and challenges. *Mol. Pharmacol.* **9**, 2380–2402 (2012).
- Duncan, R. & Gaspar, R. Nanomedicine(s) under the microscope. *Mol. Pharmacol.* **8**, 2101–2141 (2011).
- Ma, X. *et al.* Gold nanoparticles induce autophagosome accumulation through size-dependent nanoparticle uptake and lysosome impairment. *ACS Nano* **5**, 8629–8639 (2011).
- Li, J. J., Hartono, D., Ong, C. N., Bay, B. H. & Yung, L. Y. Autophagy and oxidative stress associated with gold nanoparticles. *Biomaterials* **31**, 5996–6003 (2010).
- Chen, N. *et al.* Long-term effects of nanoparticles on nutrition and metabolism. *Small* **10**, 3603–3611 (2014).
- Li, C. *et al.* PAMAM nanoparticles promote acute lung injury by inducing autophagic cell death through the Akt-TSC2-mTOR signaling pathway. *J. Mol. Cell Biol.* **1**, 37–45 (2009).
- Stern, S. T., Adisheshaiah, P. P. & Crist, R. M. Autophagy and lysosomal dysfunction as emerging mechanisms of nanomaterial toxicity. *Part. Fibre Toxicol.* **9**, 20 (2012).
- Ma, K. *et al.* Control of ultrasmall sub-10 nm ligand-functionalized fluorescent core-shell silica nanoparticle growth in water. *Chem. Mater.* **27**, 4119–4133 (2015).
- Bradbury, M. S. *et al.* Clinically-translated silica nanoparticles as dual-modality cancer-targeted probes for image-guided surgery and interventions. *Integr. Biol. (Camb.)* **5**, 74–86 (2013).
- Benezra, M. *et al.* Multimodal silica nanoparticles are effective cancer-targeted probes in a model of human melanoma. *J. Clin. Invest.* **121**, 2768–2780 (2011).
- Yoo, B. *et al.* Ultrasmall dual-modality silica nanoparticle drug conjugates: design, synthesis, and characterization. *Bioorg. Med. Chem.* **23**, 7119–7130 (2015).
- Miao, Y., Benwell, K. & Quinn, T. P. 99mTc- and 111In-labeled alpha-melanocyte-stimulating hormone peptides as imaging probes for primary and pulmonary metastatic melanoma detection. *J. Nucl. Med.* **48**, 73–80 (2007).
- Mizushima, N., Yoshimori, T. & Levine, B. Methods in mammalian autophagy research. *Cell* **140**, 313–326 (2010).
- Nelson, D. A. *et al.* Hypoxia and defective apoptosis drive genomic instability and tumorigenesis. *Genes Dev.* **18**, 2095–2107 (2004).
- Kandasamy, K. *et al.* Involvement of proapoptotic molecules Bax and Bak in tumor necrosis factor-related apoptosis-inducing ligand (TRAIL)-induced mitochondrial disruption and apoptosis: differential regulation of cytochrome c and Smac/DIABLO release. *Cancer Res.* **63**, 1712–1721 (2003).
- Jacobson, M. D. *et al.* Bcl-2 blocks apoptosis in cells lacking mitochondrial DNA. *Nature* **361**, 365–369 (1993).
- He, S. *et al.* Receptor interacting protein kinase-3 determines cellular necrotic response to TNF- α . *Cell* **137**, 1100–1111 (2009).
- Liu, Y. *et al.* Autosis is a Na⁺, K⁺-ATPase-regulated form of cell death triggered by autophagy-inducing peptides, starvation, and hypoxia-ischemia. *Proc. Natl Acad. Sci. USA* **110**, 20364–20371 (2013).
- Dixon, S. J. *et al.* Ferroptosis: an iron-dependent form of nonapoptotic cell death. *Cell* **149**, 1060–1072 (2012).
- Linkermann, A. *et al.* Synchronized renal tubular cell death involves ferroptosis. *Proc. Natl Acad. Sci. USA* **111**, 16836–16841 (2014).
- Ruhrberg, C. & De Palma, M. A double agent in cancer: deciphering macrophage roles in human tumors. *Nat. Med.* **16**, 861–862 (2010).
- Guiducci, C., Vicari, A. P., Sangaletti, S., Trinchieri, G. & Colombo, M. P. Redirecting *in vivo* elicited tumor infiltrating macrophages and dendritic cells towards tumor rejection. *Cancer Res.* **65**, 3437–3446 (2005).
- Mosser, D. M. & Edwards, J. P. Exploring the full spectrum of macrophage activation. *Nat. Rev. Immunol.* **8**, 958–969 (2008).
- Yang, W. S. *et al.* Regulation of ferroptotic cancer cell death by GPX4. *Cell* **156**, 317–331 (2014).
- Friedmann Angeli, J. P. *et al.* Inactivation of the ferroptosis regulator Gpx4 triggers acute renal failure in mice. *Nat. Cell Biol.* **16**, 1180–1191 (2014).
- Gao, M., Monian, P., Quadri, N., Ramasamy, R. & Jiang, X. Glutaminolysis and transferrin regulate ferroptosis. *Mol. Cell* **59**, 298–308 (2015).
- Gabizon, A. *et al.* Cancer nanomedicines: closing the translational gap. *Lancet* **384**, 2175–2176 (2014).

Acknowledgements

This study was funded by grants from the National Institutes of Health (R01GM111350 to M.O.; 1R01CA161280-01A1 to M.B. and U.W.; 1U54 CA199081-01 to M.B. and U.W.; R01GM113013 and R01CA166413 to X.J.; Sloan Kettering Institute Core Grant P30 CA008748CCSG and the Benjamin Friedman Research Fund to M.O.). Peptide synthesis was conducted by the University of Missouri Structural Biology Core.

Author contributions

Product preparation was performed by K.M., T.Q. and M.Z.T., experimental design by S.E.K., M.O., M.S.B., K.M., L.Z., M.Go., X.J., P.Z., S.M., F.C., T.Q. and U.W., data acquisition by S.E.K., L.Z., K.M., M.Z.T., M.Go., X.J., M.P., F.C., S.M., M.S.B., M.O., I.I.,

M.C. and M.R., data analysis and interpretation by S.E.K., M.O., M.S.B., K.M., M.P., F.C., P.Z., M.Ga., S.M., L.Z., U.W., I.I., M.C. and M.R., and preparation of the manuscript by S.E.K., M.O., M.S.B., M.Go., P.Z., K.M., S.M., T.Q. and U.W. All authors discussed the results and implications and commented on the manuscript.

Additional information

Supplementary information is available in the [online version of the paper](#). Reprints and permissions information is available online at www.nature.com/reprints. Correspondence and requests for materials should be addressed to M.S.B. and M.O.

Competing financial interests

The authors have filed an international patent application PCT/US16/34351.

Methods

Cell culture and constructs. MEF and HT-1080 cells (American Type Culture Collection, ATCC) were cultured in Dulbecco's modified Eagle's medium (DMEM, MSKCC Media Preparation Facility) supplemented with 10% fetal bovine serum (FBS, Sigma) with penicillin/streptomycin (Corning). MCF10A cells (ATCC) were cultured in DMEM/F12 (Gibco) supplemented with 5% horse serum (Atlanta Biologicals), 20 ng ml⁻¹ epidermal growth factor (Peprotech), 10 µg ml⁻¹ insulin (Sigma), 0.5 µg ml⁻¹ hydrocortisone (Sigma) and 100 ng ml⁻¹ cholera toxin (Sigma) with penicillin/streptomycin. M21 (ATCC), BxPC3 (ATCC), H1650 (ATCC) and 786-O (ATCC) cells were cultured in RPMI-1640 (Gibco) supplemented with 10% FBS with penicillin/streptomycin. Cell lines have not been authenticated, as these were purchased from ATCC, except for MEFs, which were validated with functional studies as being the correct knockouts. Cells were routinely verified as mycoplasma-free by 4,6-diamidino-2-phenylindole (DAPI) imaging. Amino-acid-free medium was prepared by dialysing heat-inactivated FBS (for MEF, HT-1080, M21, BxPC3 and H1650 cells) or horse serum (for MCF10A cells) for 4 h, followed by overnight incubation at 4 °C in phosphate-buffered saline (PBS) in MWCO 3500 dialysis tubing (21-152-9; Fisherbrand) and addition to base media prepared without amino acids. pRetro-Lamp1-GFP was introduced into M21 cells by retroviral transduction, and stable cell lines were selected with puromycin (2 µg ml⁻¹). Sample sizes for all cell studies were chosen to comply with logistical and financial constraints and they are all commensurate with the traditions of the field.

Reagents. The following reagents were used at the indicated concentrations: ConA (Sigma) 100 nM; SYTOX Green nucleic acid stain (S7020; Invitrogen) 5 nM; ferostatin-1 (Fer-1) (EMD Millipore) 1 µM; liproxstatin-1 (Selleckchem) 1 µM and 125 mg kg⁻¹ for *in vitro* and *in vivo*, respectively; deferoxamine (DFO) (Sigma) 100 µM; butylated hydroxyanisole (BHA) (Sigma) 50 µM; ascorbic acid (Asc Acid) (Sigma) 200 µM; trolox (Sigma) 100 µM; *N*-acetylcysteine (NAC) (Sigma) 10 mM; glutathione (GSH) (Sigma) 5 mM; TNFα (Sigma) 100 ng ml⁻¹; cycloheximide (CHX) (Sigma) 1 and 50 µg ml⁻¹ to induce necroptosis and apoptosis, respectively; zVAD (Sigma) 20 µM; necrostatin-1 (Sigma) 30 µM; buthionine sulfoximine (BSO) (Sigma) 400 µM; ferric ammonium citrate (FAC) (Sigma, F5879) 400 µM; erastin (Sigma), 5 µM, C11-BODIPY(581/591) 2 µM (Invitrogen). Reagents were added to cultures at the start of biological assays with the exception of ConA, which was added 1 h before lysis for western blotting.

Peptide synthesis. A modified melanocortin-1 receptor targeting peptide Re(Arg11) CCMSh¹⁴ with a double aminohexanoic acid (Ahx₂) aliphatic linker and *N*-Ac-Cys was synthesized using standard solid-phase Fmoc peptide chemistry. The rhenium-cyclized αMSH peptide analogue, Ac-Cys¹-(Ahx)₂-dLys²-Re[Cys-Cys-Glu-His-dPhe-Arg-Trp-Cys]-Arg-Val-NH₂, was analysed and purified on a Beckman Coulter high performance liquid chromatography (HPLC) system coupled with an LCQ FLEET ion trap mass spectrometer (Thermo Fisher Scientific) and finally recovered by lyophilization.

Synthesis and characterization of αMSH-PEG-C' dots. Fluorescent silica nanoparticles (C' dots) of different size, encapsulating the organic dye Cy5, were synthesized in water as previously described³⁰. αMSH peptides were conjugated to maleimido-terminated heterobifunctional PEG silane (mal-PEG-silane) via its *N*-terminal acetylated cysteine thiol to form αMSH-PEG-silane. Conjugates were attached to the particle surface in the PEGylation step as described previously^{10,30} to generate αMSH-functionalized C' dots, or αMSH-PEG-C' dots. Synthesized particle samples were dialysed in water and purified by gel permeation chromatography (GPC, Bio-Rad Laboratories) before further characterization¹⁰. Absorption and emission spectral profiles for the encapsulated and native Cy5 dye were obtained using a Varian Cary 5000 spectrophotometer (Varian) and a fluorescence spectrofluorometer (Photon Technology International). Hydrodynamic radius, brightness and concentration of αMSH-PEG-C' dots, as well as free Cy5 dye, were determined using a homebuilt fluorescence correlation spectroscopy (FCS) set-up configured with solid-state 635 nm excitation¹⁰.

Western blotting. Cells were scraped into ice-cold radioimmunoprecipitation assay buffer (RIPA) buffer (50 mM Tris at pH 7.4, 150 mM NaCl, 2 mM EDTA, 1% NP40, 0.1% SDS with protease inhibitor cocktail) and lysed for 10 min on ice. Lysates were then centrifuged at 15,870g for 20 min at 4 °C, and protein was quantified by BCA assay (Pierce). Samples were separated on 15% SDS-PAGE gels and transferred to a polyvinylidene difluoride membrane, which was blocked with tris-buffered saline plus Tween 20 (TBST) plus 5% BSA and incubated overnight at 4 °C with primary antibodies (anti-LC3A/B, 4108, Cell Signaling; anti-FTH1, 3998, Cell Signaling; anti-Actin, A1978, Sigma), diluted in blocking buffer. Blots were incubated with horseradish peroxidase conjugated to secondary antibodies, and protein was detected using enhanced chemiluminescence detection (Invitrogen). Densitometry analysis was carried out using ImageJ software (NIH).

Time-lapse microscopy. Cells were plated onto glass-bottomed dishes (MatTek) overnight, and fluorescence and differential interference contrast (DIC) images were acquired every 30 min for indicated times using a Nikon TI-E inverted microscope, a CoolSNAP HQ² charge-coupled device (CCD) camera (Photometrics), a live-cell

incubation chamber to maintain cells at 37 °C and 5% CO₂ and NIS Elements software (Nikon). Cell fates, including cell survival, death and proliferation, were manually quantified and processed using NIS Elements software and ImageJ.

Glutathione quantification. For glutathione measurements, HT-1080 cells were plated on 6 cm cell culture dishes, incubated with 15 µM αMSH-tagged nanoparticles in amino-acid-free DMEM + 10% dialysed FBS and collected ~2 h before the expected time of death. As controls, cells were treated with a mix of three parts full or amino-acid-free DMEM and 1 part H₂O, or 100 µM BSO in full media. Cells were washed three times with cold PBS and collected through cell scraping in 50 µl cold lysis buffer. Protein concentrations were measured using the BCA assay, and sample volumes were adjusted so that each had the same final protein concentration. Total glutathione was measured using the Glutathione Assay Kit (Cayman Chemicals, 703002) and reduced glutathione was measured using the QuantiChrom Glutathione Assay Kit (BioAssay Systems, DIGT-250) according to the manufacturer's instructions.

Iron measurements. For iron loading capacity measurements of C' dots, 50 µl αMSH-PEG-C' dots (60 µM) were added to either 150 µl iron-containing media (8.6 µM) or 150 µl FeCl₃ solutions prepared over a range of iron (Fe³⁺) concentrations (2 µM to 2 mM, Supplementary Table 1). Solutions were spun at room temperature (160 r.p.m.) for 48 h, followed by separation of free iron from C' dots using a PD-10 column and eluting in water. Cellular samples were incubated with and without particles in media for 48 h before centrifugation, pelleted and washed three times before re-suspending in PBS solution. Iron measurements (parts per billion, ppb) were determined using a microwave plasma - atomic emission spectroscopy, along with iron-loading capacities. Iron loading capacity was computed as the ratio of the amount of iron in purified particle-exposed C' dots (or cells), divided by the total amount of initial iron measured before purification and multiplied by 100. All experiments were performed in triplicate.

GPX4 activity assay. The GPX4 specific activity assay was performed according to ref. 31. In brief, frozen cell pellets were resuspended in 100 µl lysis buffer (100 mM KH₂PO₄/K₂HPO₄, pH 7.4, 1 mM EDTA, 150 mM KCl, 0.1% CHAPS, 3 mM β-mercaptoethanol and protease inhibitor cocktail) and homogenized by 50 pestle strokes. Samples were incubated for 15 min on ice, and cell debris was removed by centrifugation (20,000g, 10 min, 4 °C). A quantity (50 µl) of the supernatant from homogenized cells was used to measure the enzymatic activity in 1 ml of assay buffer (100 mM Tris HCl pH 7.8 containing 5 mM EDTA, 0.1% Triton X, 3 mM GSH, 200 µM NADPH and 0.6 U ml⁻¹ glutathione reductase) in the presence of 20 µM phosphatidylcholine hydroperoxide (PCOOH). GPX4 activity was determined by the glutathione reductase-dependent consumption of NADPH detectable by a decrease in absorbance at 340 nm in a SpectraMax plate reader (Molecular Device). Protein content in the samples was determined by the colorimetric 660 nm Pierce protein assay method.

Animal models and tumour inoculation. All animal experiments were performed in accordance with protocols approved by the Institutional Animal Care and Use Committee of Memorial Sloan-Kettering Cancer Center and followed NIH guidelines for animal welfare. Human melanoma (M21) xenografts were generated on the shaved flanks of immunodeficient male severe combined immunodeficiency (SCID)/Beige C.B-17/IcrHsd-Prkdc^{scid}Lysf^{bg}-1 mice (6–8 weeks old, Harlan Laboratories). Human sarcoma HT-1080 and 786-O flank xenografts (~2.0 × 10⁶ cells per 100 µl) were also generated in the same model. Average initial tumour volumes of 45–75 mm³ were used for all studies. For all *in vivo* studies, three animals per group were used. No randomization was used and no blinding was performed.

***In vivo* dosing strategy and examination.** Five million M21 cells, cultured in serum-supplemented media, were subcutaneously implanted into the right flank of mice using a 23-gauge trocar needle to establish melanoma xenografts 2 days after particle exposure (*n* = 3) or without exposure (*n* = 3). In a subsequent study, mice were assigned to one of two different treatment groups to evaluate the response of HT-1080 and 786-O tumours to high concentrations (60 µM) of i.v.-injected αMSH-PEG-C' dots (*n* = 5 mice; 200 µl) administered three times over a 10 day period (that is, days 0, 4 and 7). Control HT-1080 and 786-O mice (*n* = 3) were administered with 0.9% saline vehicle at the same time points. In a third treatment study, HT-1080 mice were assigned to one of two groups to evaluate the response to three, high-concentration doses (60 µM) of i.v.-injected αMSH-PEG-C' dots (*n* = 3 mice; 200 µl) alone or following i.p. administration of liproxstatin-1 (*n* = 3 mice, 125 mg kg⁻¹) over a 10 day period. Tumour sizes were measured using calipers over the treatment interval. All mice were examined by palpation at the site of tumour cell inoculation and were observed daily until the termination of tumour growth studies for signs of morbidity or mortality. Two perpendicular diameters (*d*₁ ≤ *d*₂) of the tumour used to calculate the tumour volume ($V = 4/3 \times \pi \times d_1^2 \times d_2/8$) were measured with calipers daily following the injection of cells.

***In vivo* fluorescence imaging.** Animals were anesthetized using isoflurane, and whole-body optical fluorescence imaging was acquired to identify nanoparticle

fluorescence at the tumour site. Mice were scanned for 0.1–1 s using the IVIS Spectrum photon-counting device optical imaging system (Xenogen) with the blocks and filters for Cy5 fluorescence (excitation 650 nm, emission 680 nm) and for background fluorescence (excitation 465 nm, emission 600 nm), selected according to the manufacturer's recommendations. The fluorescence background was subtracted according to the manufacturers' instructions. Fluorescence signal was reported as radiant efficiency ((photons $s^{-1} cm^{-2} sr^{-1}$) $\mu W^{-1} cm^{-2}$).

Histopathological analysis. Immediately after terminating the *in vivo* imaging study, HT-1080 and 786-O male and female mice were euthanized by CO₂ inhalation, and representative particle-exposed ($n = 2$) and control ($n = 1$) tumours, as well as hepatic and renal specimens, were excised at necropsy. Haematological specimens were also obtained for complete blood counts and serum chemistries. Excised tumours, livers and kidneys were fixed in 10% neutral buffered formalin for 24 h, processed in alcohol and xylene, embedded in paraffin, sectioned at 5 μm thickness, and stained with haematoxylin and eosin (H&E). Additional tumour sections were stained by immunohistochemistry for Mac-2 (primary antibody Cedarlane CL8942B applied at a concentration of 1:100 following heat-induced epitope retrieval (HIER) in a pH 6.0 buffer), myeloperoxidase (Dako A0398, 1:1,000, HIER pH 6.0), cleaved caspase-3 (Cell Signaling Technology 9661, 1:250, HIER pH 6.0) and Ki-67 (Abcam ab16667, 1:100, HIER pH 9.0). Mac-2 staining was performed manually with an avidin-biotin detection system (Vectastain ABC Elite Kit, Vector Laboratories, PK-6100). Other stains were performed on a Leica Bond RX automated stainer using the Bond Polymer Refine detection kit (Leica Biosystem DS9800). Tumour sections were also stained by the terminal deoxynucleotidyl

transferase dUTP nick-end labelling (TUNEL) method as previously described. All slides were examined by a board-certified veterinary pathologist.

Tumour vascularity assessment. Tumour vascularity was assessed by staining HT-1080 tumours by immunohistochemistry for CD31 on a Leica Bond RX automated staining platform (Leica Biosystems). Following heat-induced epitope retrieval at pH 9.0, the primary antibody (rat monoclonal, catalogue no. DIA-310, Dianova) was applied at a concentration of 1:250 and was followed by application of a polymer detection system (Novocastra Bond Polymer Refine Detection, Leica Biosystems).

Statistics. Volume–time profiles were compared between the two treatment groups using robust standard errors calculated by a generalized estimating equations approach³². Particle-treated tumour growth profiles, with and without a pharmacological inhibitor to ferroptosis, liproxstatin-1, were compared using a linear model. The longitudinal aspect of the data was taken into account using GEEs. We assigned statistical significance at $P < 0.05$.

References

30. Ma, K., Zhang, D., Cong, Y. & Wiesner, U. Elucidating the mechanism of silica nanoparticle PEGylation processes using fluorescence correlation spectroscopies. *Chem. Mater.* **28**, 1537–1545 (2016).
31. Roveri, A., Maiorino, M. & Ursini, F. Enzymatic and immunological measurements of soluble and membrane-bound phospholipid-hydroperoxide glutathione peroxidase. *Methods Enzymol.* **233**, 202–212 (1994).
32. Zeger, S. L., Liang, K. Y. & Albert, P. S. Models for longitudinal data: a generalized estimating equation approach. *Biometrics* **44**, 1049–1060 (1988).